AGU PUBLICATIONS

JGR

Journal of Geophysical Research: Oceans

RESEARCH ARTICLE

10.1002/2015JC010746

Key Points:
- Skin temperature length scales are linearly correlated with depth
- Surface and subsurface dissipation rates and currents are highly correlated
- Surface length scales and mean flow scale with subsurface dissipation

Correspondence to:
S. E Brumer,
sbrumer@ldeo.columbia.edu

Citation:
Brumer, S. E., C. J. Zappa, S. P. Anderson, and J. P. Dugan (2016), Riverine skin temperature response to subsurface processes in low wind speeds, *J. Geophys. Res. Oceans*, *121*, doi:10.1002/2015JC010746.

Received 27 JAN 2015
Accepted 8 FEB 2016
Accepted article online 12 FEB 2016

Riverine skin temperature response to subsurface processes in low wind speeds

Sophia E. Brumer[1], Christopher J. Zappa[1], Steven P. Anderson[2], and John P. Dugan[2]

[1]Lamont-Doherty Earth Observatory, Columbia University, Palisades, New York, USA, [2]Areté Associates, Arlington, Virginia, USA

Abstract Both surface and subsurface processes modulate the surface thermal skin and as such the skin temperature may serve as an indicator for coastal, estuarine, and alluvial processes. Infrared (IR) imagery offers the unique tool to survey such systems, allowing not only to assess temperature variability of the thermal boundary layer, but also to derive surface flow fields through digital particle image velocimetry, optical flow techniques, or spectral methods. In this study, IR time-series imagery taken from a boat moored in the Hudson River estuary is used to determine surface flow, turbulent kinetic energy dissipation rate, and characteristic temperature and velocity length scales. These are linked to subsurface measurements provided by in situ instruments. Under the low wind conditions and weak stratification, surface currents and dissipation rate are found to reflect subsurface mean flow ($r^2 = 0.89$) and turbulence ($r^2 = 0.75$). For relatively low dissipation rates, better correlations are obtained by computing dissipation rates directly from wavenumber spectra rather than when having to assume the validity of the Taylor hypothesis. Furthermore, the subsurface dissipation rate scales with the surface length scales (L) and mean flow (U) using $\varepsilon \propto \frac{U^3}{L}$ ($r^2 = 0.9$). The surface length scale derived from the thermal fields is found to have a strong linear relationship ($r^2 = 0.88$) to water depth (D) with $(D/L) \sim 13$. Such a relation may prove useful for remote bathymetric surveys when no waves are present.

1. Introduction

In alluvial and coastal waters, turbulence is driven both by wind forcing at the air-water interface and friction at the bottom boundary layer. In such environments, tidal flow enhances near-surface turbulence through shear over topography and can be the dominant driver of turbulent kinetic energy in low to moderate wind regimes [*Zappa et al*., 2003, 2007]. In a shallow, weakly stratified water column, bottom-generated turbulence may propagate to the surface and result in distinct coherent features observable at the surface under low wind conditions. When winds exceed ~5 m/s and the tidal flow is low, winds become the dominant driver of turbulence in the upper boundary layer and the air-water interface is dominated by wind stress and other near-surface secondary flows such as Langmuir circulation [*Leibovich*, 1983; *Melville et al*., 1998; *Veron and Melville*, 2001].

The large-scale surface signatures of bottom-generated turbulence are termed boils. They are thought to be produced by upwelling water which, upon impinging on the surface, spreads radially. Boils are discernable in visible imagery as the upwelled water is sediment laden. They are also associated with regions of increased bubble concentration and can be detected in sonograph images [*Nimmo-Smith et al*., 1999]. Observations of boils have been reported both for relatively shallow rivers [*Jackson*, 1976; *Talke et al*., 2013] and the shallow tidal North Sea [*Nimmo-Smith et al*., 1999].

The analysis of bottom-generated turbulence over riverbeds dates back to shortly after World War II [*Matthes*, 1947]. It has since been recognized that large-scale vortical motions are omnipresent forms of turbulence in rivers and estuaries. The evolution of an ideal turbulent eddy in the wall region of a turbulent boundary layer was described by *Allen* [1985]. In turbulent boundary layer flow, velocity increases away from solid boundary and momentum in continuously exchanged from the outer flow towards the boundary. At the wall, low momentum fluid is periodically gathered into coherent structures which are subsequently pulled or thrusted upward into the faster outer current. As the upper portion moves faster than that near the bed, the coherent structure becomes wedge shaped. As it grows in height, the fluid in the lower lee is

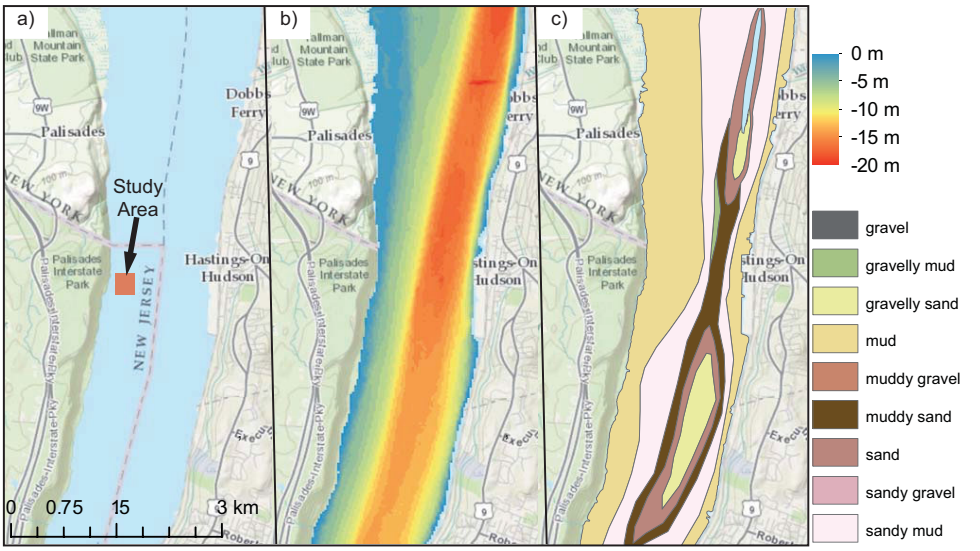

Figure 1. (a) Map of the Hudson River estuary. The study area is highlighted in red. (b) Bathymetric map derived from soundings collected between 1930 and 1945, and fed into a Digital Elevation Model with 30 m resolution by NOAA. (c) Map showing riverbed sediment types determined from interpretation of sediment size measured from cores and grabs by *Bell et al.* [2006].

increasingly sheltered and the coherent structures are increasingly sheared. Viewed from above, the coherent structure resembles an elongated horseshoe or hairpin with the center portion that is the farthest from the boundary moving the fastest and furthest and the flanks being carried forward less rapidly. The generation of coherent structures and boils over river dunes is reviewed by *Best* [2005].

Bubble or dye injection experiments showed evidence of vertical streaks in the innermost turbulent boundary layer [*Grass*, 1971; *Kline et al.*, 1967]. These low speed streaks are locally and intermittently subject to a cyclic process described as bursting [*Kline et al.*, 1967]. The burst cycles generated in the bottom boundary layer have been described in two comparable conceptual models [*Offen and Kline*, 1975] illustrated in Figures 1 and 2 in *Jackson* [1976]. In these models, the boundary layer is subdivided in an inner zone and an outer zone. The outer region can be further subdivided into zones of uniform momentum or into an intermediate region and a surface influenced region [*Adrian et al.*, 2000; *Hurther et al.*, 2007; *Nezu and Nakagawa*, 1993].

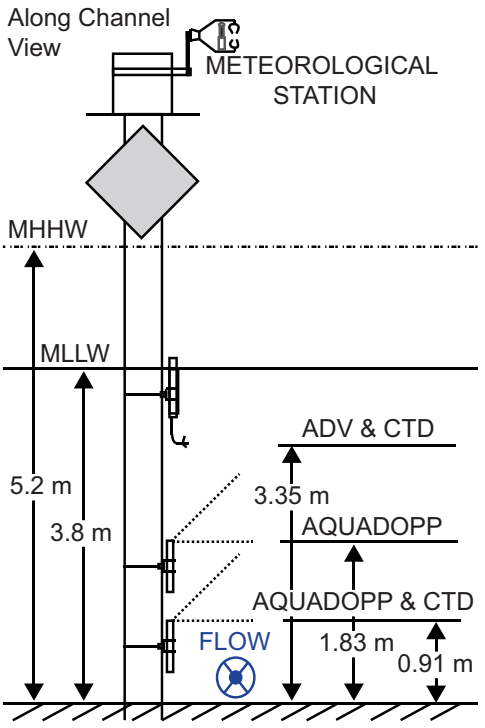

Figure 2. An along channel schematic of the in situ instrumentation set up on the pilling.

The majority of the turbulence is produced in the inner zone in which the innermost viscous layer is made of low speed streaks that are periodically lifted up by transverse vortices that arise from the high flow shear at the boundary between the zones. The lifted streak grows, as do the vortices, until it breaks up creating a burst. Being a buffer layer process, the bursting phenomenon involves inner scales that are an order of magnitude smaller than outer scales [*Hurther et al.*, 2007]. *Heathershaw* [1974] made measurements of near bottom turbulence in the Irish Sea and showed evidence of bursts in time series of turbulent velocity fluctuations. *Matthes* [1947] labeled the upward-tilted stream wise vortices that arise from bursts as "kolks." These kolks ultimately result in boils when reaching the surface.

Differing views have emerged as to the evolution of the vortices or eddies after their generation. *Yalin* [1992] suggested that these grow almost to the vertical extent of the water column before breaking up into new eddies whereas *Shvidchenko and Pender* [2001] reported depth scales eddies which remain frozen in the flow. Whether there is cyclic growth and destruction of eddies leading to surface velocity fluctuations or whether these arise from ordered sequences of 3-D eddies moving with the bulk flow has important implications as to the relation between surface scales, depth and velocity as well as surface renewal.

How the turbulence generated at the river bed affects the water column and subsequently the surface determines the nature of the surface indicators detected by remote sensing. There is extensive literature on bottom-generated turbulence and free stream turbulent near plane boundary, especially with regards to sediment transport [e.g., *Gordon*, 1975*; Grass*, 1971*; Matthes*, 1947*; Vanoni and Hwang*, 1967]. Most studies rely on visual observation and only recently have efforts been made to link bottom-generated turbulence to InfraRed (IR) observations [*Chickadel et al*., 2011; *Talke et al*., 2013; *Zappa et al*., 2003].

IR imagery allows for measurements of the skin temperature. The skin temperature is governed by both surface and subsurface processes. The net air-water heat flux typically leads to a cooler thermal boundary layer (TBL) compared to the underlying bulk layer. Even a modest net surface heat flux leads to a detectable IR signal, which makes IR remote sensing possible both during day and night. In the open ocean, the temperature difference skin and the interior is typically 0.2°C [*Katsaros*, 1980; *Liu and Businger*, 1975; *Saunders*, 1967]. Turbulent motions resulting from wind forcing at the air-sea interface and from turbulent eddies generated within the water column, disrupt the TBL, mixing it with the bulk layer. In the open ocean, surface temperature modulation can be associated with large scale processes such as surface and internal gravity waves [*Farrar et al*., 2007; *Veron et al*., 2008, 2009; *Zappa and Jessup*, 2005]. In channel flows such as estuaries or river, a variety of phenomena lead to disruption of the TBL and even total removal of the TBL for short periods of time [e.g., *Zappa et al*., 2004; *Chickadel et al*., 2009; *Plant et al*., 2009; *Smith et al*., 2001]. The large surface divergence associated with boils leads to disruption of the TBL.

Here we aim to infer characteristics of subsurface turbulence and bulk water properties from skin temperature measurement. The study is based on infrared imagery recorded at nighttime under low wind conditions from a barge in the Hudson River. A strong relationship between surface length scales derived directly from infrared imagery and water column depth is shown to exist under low wind conditions when the TBL is dominated by bottom-generated turbulence. Under such conditions, we find surface velocities derived from IR time-series imagery correspond to subsurface current velocities. Furthermore, we find turbulent kinetic energy dissipation rates calculated directly from wavenumber spectra of surface velocity fields correlate with subsurface dissipation rates. Finally, we show how subsurface dissipation may be inferred from surface currents and length scales. The paper is organized as follows: the study area and field campaign is briefly described in the methods section; the methods section also contains the data processing procedure; results are described in section 3 and discussed in section 4.

2. Methods

2.1. Study Area

The field campaign was undertaken in the Hudson River estuary on the nights of 18 and 19 November 2010. The study area, shown in Figure 1, was located by the State Line Lookout in the Palisades Interstate Park, NJ, ~32 km north of Manhattan. The data collection was made outside of the tidal channel, in a region of relative uniformity over a muddy riverbed, where the water depth, inferred from the pressure sensors of subsurface instruments, varied between 3.8 and 5.2 m during the survey period. Higher resolution bathymetry (not shown) confirms lack of bed forms in the study region. The Hudson River estuary is microtidal with a semidiurnal tidal range of ~1.4 m and tidal currents of ~1-2.5 m s^{-1} (values at Dobbs Ferry, taken from http://tidesandcurrents.noaa.gov/). The mean tidal discharge varies from about 12,000 m^3s^{-1} at The Battery where the Hudson flows into New York Harbor to zero at Troy [*Abood*, 1974]. River discharge estimates are only available in the freshwater part of the Hudson, the southernmost being below Poughkeepsie (USGS 01372058), where the discharge was of 991 m^3s^{-1} on the 18th and 728 m^3s^{-1} on the 19th.

2.2. Data and Instrumentation

A series of 10 min IR videos were taken of the river surface from a crew boat (Marguerite Miller, from Miller's Launch) moored in proximity of a pilling on which various instruments were mounted. The IR data were collected every 30 min between 0100–0600 UTC on the 18th (year day 322), and 0400–1000 UTC on the 19th (year day 323) amounting to a total of 23 runs. Surface and subsurface in situ instruments mounted on the piling provided measurements of environmental parameters such as wind speed, heat fluxes, air and water temperatures, humidity as well as subsurface currents, turbulence, and salinity (Figure 2).

The IR camera used, was a CEDIP Jade III longwave (7.7–9.3 μm) camera which was mounted on a pan/tilt system on the A-frame of the moored ship. This setup permitted movement of the camera with the current as to always have a vantage point upstream of the ship. The camera was mounted at ∼5.5 m above the water level with and incidence angle of about 25°. An Xsens IMU (Inertial Measurement Unit) mounted on the pan/tilt system next to the camera measured the roll and pitch of the boat motion at a frequency of 10 Hz, allowing for projection correction. The field of view angles of the camera are 21.7° × 16.4° giving an image area of 4.57 m^2 with an average pixel size of 0.59 cm^2. The CEDIP Jade III offers better than 15 mK temperature resolution, 14 bit digitization, and 320 × 240 pixels resolution. The sampling frequency was set to 60 Hz.

The atmospheric boundary layer was measured with a Campbell air-sea flux package. This meteorological station was mounted on the piling neighboring the ship at a height of 7.5 m above the river bed. It provided measurements of wind speed and direction, relatively humidity, atmospheric pressure, air temperature, solar insolation, and downwelling longwave radiation. In situ subsurface instrumentation (Figure 2) consisted of among others a 2 MHz Nortek model Vector ADV, mounted on the aforementioned piling at 3.35 m above the riverbed. The ADV collected data in 10 min bursts at the top of every $^1/_2$ h, with a sampling frequency 32 Hz. Additionally, two high resolution 2 MHz Nortek model Aquadopp profilers were mounted on the piling at 0.91 m and 1.83 m above the riverbed. The Aquadopps measured velocity fluctuations along three beams with a 25 mm spatial resolution over 0.75 m. The two horizontal beams were nominally at 45° from the mean flow. The profilers collected data in 59 min bursts at the top of every hour, with a sampling frequency 2 Hz. Currents were also measured by a bottom-mounted upward-looking 1200 kHz RDI ADCP. The ADCP was located 35 m to the northwest of the pilling. The ship remained within 130 m of the pilling and 100 m of the ADCP during data collection. The ADCP provided velocities over vertical bins are 25 cm apart, starting at 81 cm above the riverbed at a frequency of 1 Hz. 2 CTDs were mounted on the piling at 99.4 cm (3″) and 3.35 m (11″) above the river bed, sampling at 0.5 Hz. CTD profiles were also taken from the side of the barge before and after each IR video. All instruments mounted on the piling were oriented toward the middle of the river channel and were never in the wake of the piling under any flow conditions.

2.3. Surface Current Retrieval

Surface velocity fields were been determined by two approaches:

1. Feature tracking or Digital Particle Velocimetry (DPIV)
2. From the advective surface in 3-D spectra of the skin temperature (SAS)

The feature tracking DPIV method is based on 2-D spatial cross-correlations ($\phi_{fg}(x,y)=f\ o\ g=\sum_{i=0}^{I-1}\sum_{j=0}^{J-1} f(i,j)g(x+i,y+j)$) between 16 × 16 pixels correlation windows in a first frame and 32 × 32 pixel search window in a second frame. The two frames are consecutive, taken 1/10th of a second apart. Velocities are determined on nodes spaces eight pixels apart in the *x* and *y* direction. The distance between the centers of the windows and the location of the maximum cross-correlation (MCC) divided by the time between image A and B give the magnitude of the current speed and the vector connecting centers to MCC gives the direction of the displacement. The location of the MCC is approximated with two 3-point Gaussian curve fits, one in each direction so as to improve the subpixel accuracy. MCC-based surface current retrievals from IR time-series imagery have been shown to be successful in riverine environments [e.g., *Puleo et al.*, 2012; *Dugan et al.*, 2014]. Performing the cross-correlation in the spatial domain is numerically more intensive than computing it in the frequency space via a Fast Fourier Transform. However, it is more accurate and flexible [*McKenna and McGillis*, 2002].

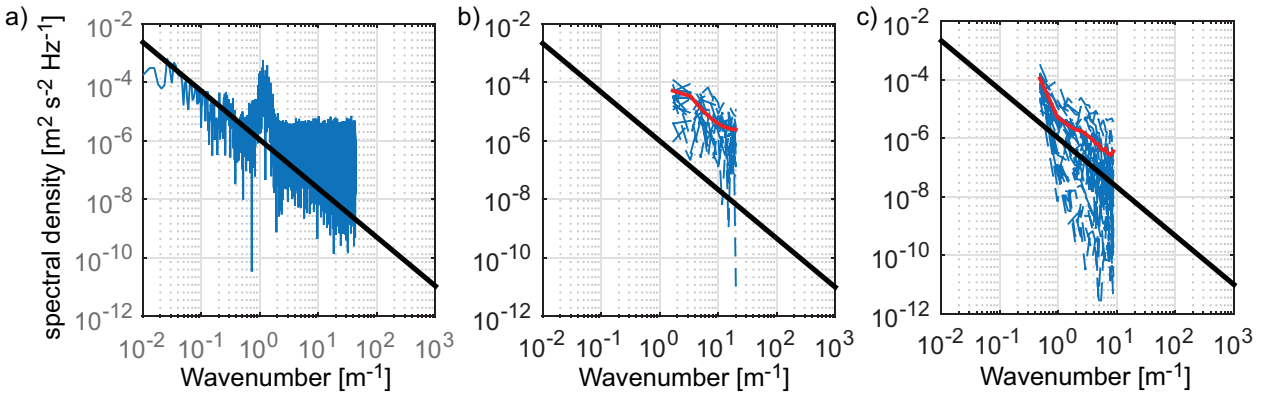

Figure 3. Examples of wavenumber spectra computed from (a) the ADV, (b) the bottom Aquadopp, with individual profiles in blue and a 10 min mean in red, and (c) DPIV surface velocity fields, in blue for an individual row and in red a frame mean. The solid black line represents the $k^{-\frac{5}{3}}$ slope.

The advective surface approach is based on *Dugan and Piotrowski* [2012] method. They showed how to determine the surface flow magnitude and direction by fitting the 2-D planar surface, which arises from advective variance detectable in 3-D spectra of airborne visible imagery. Computing 3-D spectra of the every 3000 frames of each run, the advective signal is clearly visible. For less than 3000 frames, the energy of advective signal tends to be too low. A linear least square fit of the advective surface in wavenumber frequency slices of the 3-D spectra was performed at various angles relative to the image. The slope of the linear fit is the magnitude of the advection at a given angle. Fitting a cosine function to the obtained magnitudes as a function of angle, we determine the magnitude and direction of the surface flow as the maximum of the fit and the corresponding angle.

2.4. Turbulent Kinetic Energy Dissipation

The turbulent kinetic energy (TKE) dissipation rate ε is estimated by fitting the inertial subrange of wavenumber spectra ($\Phi(k)$) with a $k^{-5/3}$ slope following the Kolmogorov turbulence cascade which dictates that:

$$\Phi(k) = \alpha \varepsilon^{\frac{2}{3}} k^{-\frac{5}{3}}$$

where k denotes the wavenumber and α is a constant equal to 1.5. Wavenumber spectra were computed directly from both the IR-derived velocity fields and Aquadopp profiles (cf. Figure 3). For time series measurement of velocities such as collected by ADVs, one has to make a further assumption before deriving TKE dissipation rates. Assuming that the frozen Taylor hypothesis is valid, i.e., that turbulent eddies remain unchanged while being advected by the mean flow, one can convert frequency spectra $S(f)$ into wavenumber spectra as follows:

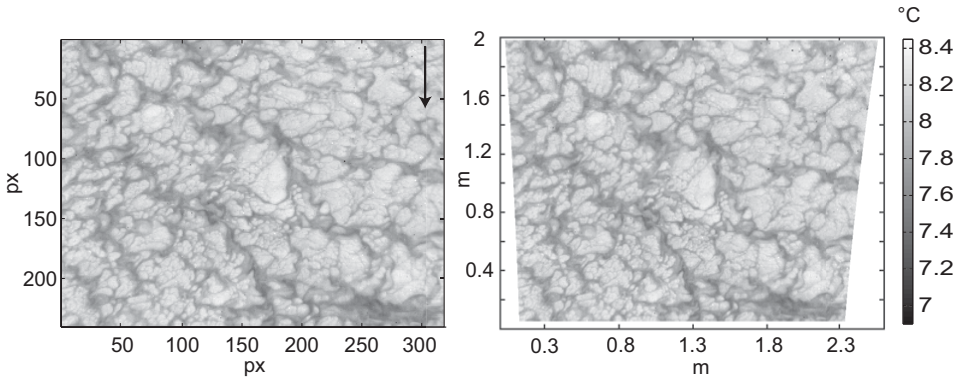

Figure 4. (a) An example of a calibrated IR image preprojection correction; the black arrow indicates the mean flow direction. (b) The same frame scaled and projected correctly.

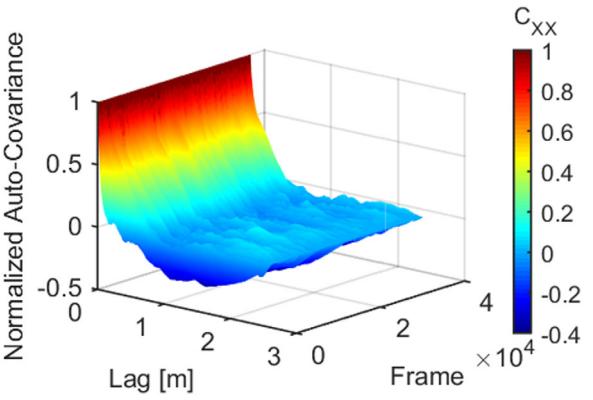

Figure 5. Sample time series of the frame averaged normalized spatial autocovariance (C_{XX}) of the thermal imagery for various lags. The color map reflects the autocovariance.

$$\Phi(k) = S(f).\frac{\langle v \rangle}{2\pi},$$

$$with\ \ k = 2\pi f / \langle v \rangle$$

where f is the frequency and $\langle v \rangle$ the mean velocity.

2.5. Surface Length Scales

Characteristic surface length scales are determined directly from the skin temperature imagery and from the DPIV velocity fields from which the frame mean velocity was removed. In order to do so, it is necessary to scale the imagery and transform the camera coordinates to water level coordinates. This is achieved through a rotation matrix using the roll, pitch, and yaw angles measured by the IMU as exemplified in Figure 4.

From the scaled fields, normalized autocovariance functions were computed for each row and column of each frame (an example of which is shown in Figure 5). The normalized autocovariance is given by: $C_{XX}(\delta) = \frac{\sum_{p=0}^{P-\delta} x(p)x(p+\delta)}{\sum_{p=0}^{P} x(p)^2}$, where δ is the lag, P is the number of pixels in a row or column, and $x(p)$ is the temperature of a given pixel. For each frame, two mean normalized autocovariance functions were subsequently computed, one for each dimension. Characteristic skin temperature length scales (*L1* and *L2*) were determined as the distance at which the skin temperatures are no longer correlated, i.e., corresponding to the smallest lag at which the frame mean autocovariance function are equal to zero. From the DPIV fields, we first computed four length scales, one for each component of the velocity vector for both dimensions of the image which were averaged to give one single scale for each run.

3. Results

3.1. Environmental Conditions Including Surface and Subsurface Currents

IR measurements were taken under varying wind conditions, with 30 min average wind speed ranged from 0.12 to 3.62 m s^{-1} (Figure 6). The wind speed averaged 2.29 $\pm$ 1.31 m s^{-1} on the night of the 18th (year day 322) and 1.06 $\pm$ 0.67 m s^{-1} on the night of the 19th (year day 323). As a result, the momentum flux was much stronger on the 18th with a mean and standard deviation of 0.30 $\pm$ 0.23 kg m^{-1} s^{-2}; on the 19th it only reached 0.13 $\pm$ 0.08 kg m^{-1} s^{-2}.

Measurements coincided with the ebbing tide on the first night and low water to flood tide during the second night (Figure 7a). An estimate of the bulk current speed was obtained by computing a column averaged velocity from the ADCP from the deepest bin (81 cm above the river bed) to the top good bin about 50–75 cm below the water surface. A time series of the column-averaged velocity is plotted in Figure 7a and 10 min-averaged velocity corresponding to periods of imagery recording are reported in Table 1. Over

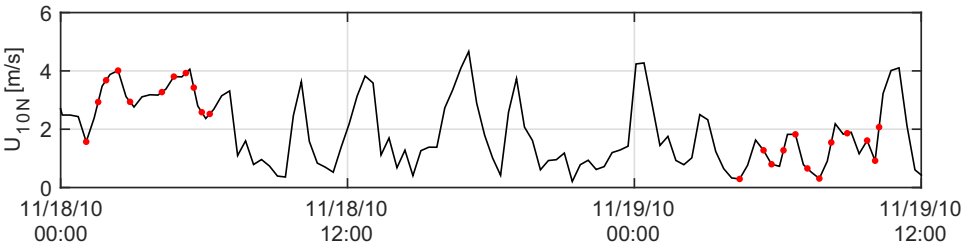

Figure 6. Time series of the 20 min averaged U10 neutral measured by the meteorological station on the piling, the red dots represent the IR data collection periods.

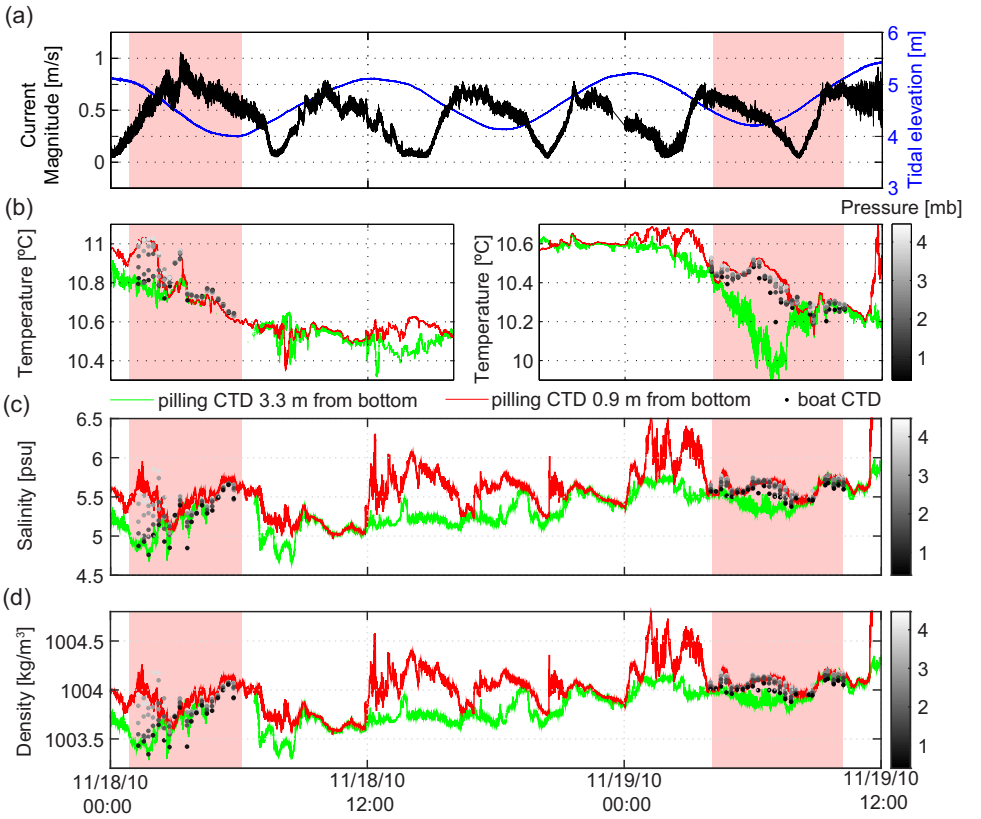

Figure 7. Time series of (a) column-averaged currents and tidal elevation given by the ADCP, (b) measured temperature, (c) measured salinity, and (d) derived density from the two CTD mounted on the pilling at 3.3 (green) and 0.9 (red) meters from the bottom, respectively, as well as from the CTD profiles taken from the barge. The pink-shading delimits the periods of IR measurements. At the end of the first night and toward the middle of the second night, the surface CTD (mounted 3.3 m above the river bed) was out of the water leading to erroneous measurements which were excluded from the graphs.

the time period IR imagery was recorded, the 10 min-averaged current speed measured by the ADCP ranged from 0.07 to 0.73 m s^{-1}. These strongly correlated to the 10 min average ADV measurements ($r^2 = 0.9$, cf. Figure 8a). Even though one could expect the surface flow to be wind driven, the winds experienced were so weak that the surface velocities derived from the imagery match the column-averaged ADCP ($r^2 = 0.89$ for SAS and $r^2 = 0.82$ for DPIV, cf. Figure 8b and 8c) velocities and ADV velocities ($r^2 = 0.79$ for SAS and $r^2 = 0.71$ for DPIV). Surface currents matching subsurface flow may be expected in a tidally forced system in extremely low winds. The surface velocities were also found to correlate with the bottom ADCP measurements ($r^2 = 0.78$ for SAS and $r^2 = 0.68$ for DPIV). Both surface current retrieval methods agree very well with an $r^2 = 0.95$.

Table 1. Table of the 10 min Column-Averaged ADCP Current Magnitude (*U*), Flow Direction, Depth (*D*), the Bulk Reynolds Number ($Re = \frac{UD}{\nu}$), the Turbulent Reynolds Number ($Re_T = \frac{UL}{\nu}$), Mean Decorrelation Length-Scale (*L*), Mean Length-Scale Roughly Perpendicular to the Flow (*L1*) and Mean Scale Roughly Parallel to the Flow (*L2*).

U (m s^{-1})	*U* direction to	Depth (m)	*Re*	Re_T	*L* (cm)	*L1* (cm)	*L2* (cm)
0.27	W	5.05	1.35E + 06	1.07E+05	40.1 ± 5.6	26.8 ± 5.5	53 ± 8.2
0.56	W	4.27	2.38E + 06	1.85E + 05	33.1 ± 5.3	30.5 ± 5.1	35.5 ± 8.3
0.41	W	4.23	1.72E + 06	1.29E + 05	31.7 ± 6.1	24.5 ± 5.2	39.2 ± 8.5
0.31	W	4.29	1.33E + 06	8.68E + 04	28.1 ± 5.8	21.8 ± 4.4	34.8 ± 0.6
0.2	W	4.37	8.75E + 05	6.81E + 04	34.1 ± 7.9	29.8 ± 5.6	38.4 ± 12.8
0.07	W	4.49	3.12E + 05	2.35E + 04	34 ± 8.0	30.5 ± 4.9	37.6 ± 12.9
0.29	NE	4.69	1.36E + 06	1.10E + 05	37.8 ± 6.0	30.4 ± 5.0	45.2 ± 8.8
0.67	ENE	4.94	3.30E + 06	2.61E + 04	39.1 ± 5.6	31 ± 4.5	47 ± 7.9
0.67	ENE	5.02	3.35E + 06	2.88E + 04	43.2 ± 7.2	34.9 ± 5.5	50.9 ± 10.2
0.7	ENE	5.09	3.56E + 06	3.05E + 04	43.5 ± 7.3	34.5 ± 7.1	51.9 ± 8.2

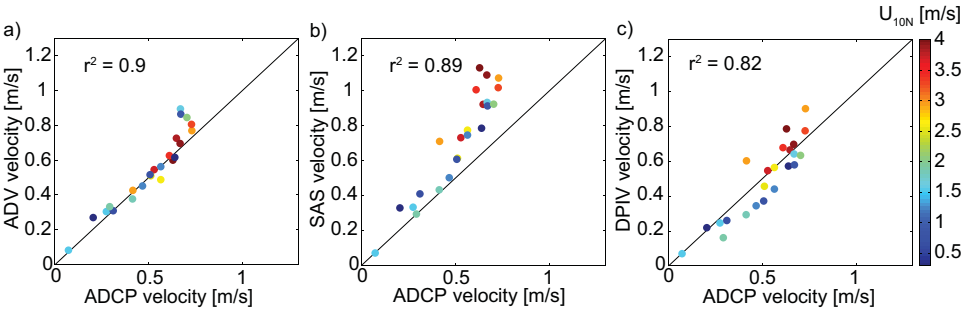

Figure 8. Scatter plots of the run mean flow magnitudes derived from the ADCP versus the (a) ADV, (b) SAS, and (c) DPIV. The data are color-coded according to wind speed (U_{10N}). The 1:1 line is shown in black.

Subsurface turbulence was strong enough for the water column to be well mixed throughout the majority of the IR imaging measurement period as seen in Figure 7. Only during the first couple of runs does, there appear to be a small degree of stratification (see Figure 7d). The column mean Brunt-Vaisala frequency ($N=\sqrt{\frac{g}{\rho_0}\frac{d\rho(z)}{dz}}$) calculated during IR imagery was recorded was of 0.0327 ± 0.0259 s^{-1} based on the pilling CTDs and of 0.0194 ± 0.001 s^{-1} based on the CTD casts taken from the barge Figure 9 shows the mean profile of N^2 (times 4) based on the CTD casts. Several data points and profiles were removed from the analysis as they correspond to periods of time when thermal reflections contaminated the infrared imaged surface temperature field. These data are excluded from data presented in Figures 9–12. This eliminated all but the first run of the first night of measurements as well as two runs taken during the second night. Such low buoyancy frequency reinforces the idea of a weakly stratified water column. The Richardson number ($Ri=\frac{N^2}{\left(\frac{du}{dz}\right)^2}$) calculated from the pilling and boat CTDs and the ADCP was below the critical Richardson number of ¼ throughout most of the survey. This is indicative of a turbulent flow regime where shear can overcome the stabilizing effects of the stratification. Only during the first three runs did the Ri go above critical; increasing from 0.4 in run 1– 0.77 in run 2 and decreasing to 0.55 in run 3. The shear determined from the ADCP was relatively uniform within the water column; averaging 0.003 s^{-2} with signs of enhanced shear (0.005–0.013 s^{-2}) toward the bottom of the water column (Figure 9). Experimental set up did not allow for an estimate of the shear in the bottom boundary, the deepest velocity measurement being at 81 cm above the river bed.

During the low water period on 18 November, the CTD mounted to the piling 3.3 m above the riverbed emerged above the water level and was exposed to the atmosphere leading to erroneous measurements. These were excluded from Figure 7. The CTD profiles taken from the barge closely follow the measurements taken at the pilling confirming the horizontal homogeneity of the study site and the low level of stratification.

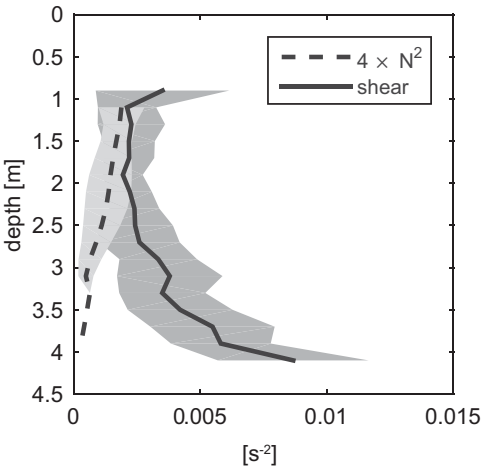

Figure 9. Mean profiles of four times the buoyancy frequency determined from shipborne CTD casts (dashed line) and shear computed from the ADCP (solid line). The light and dark gray shadings indicate the one standard deviation bounds for the buoyancy frequency times 4 and the shear, respectively.

3.2. Turbulent Kinetic Energy Dissipation

Surface-derived TKE dissipation rates correlate with the subsurface dissipation rates (cf. Figure 10). As described in section 2.4, both DPIV and Aquadopp TKE dissipation rates were computed directly from wavenumber spectra, whereas the ADV TKE dissipation rates were derived from frequency spectra assuming the validity of the Taylor hypothesis of frozen flow. All runs with reflection have been discarded since they generate unreliable DPIV fields. Since the TKE dissipation rates range over several orders of magnitude, computing a linear correlation coefficients gives a biased result reflecting mostly the tightness of fit of the higher values. In order to avoid that bias,

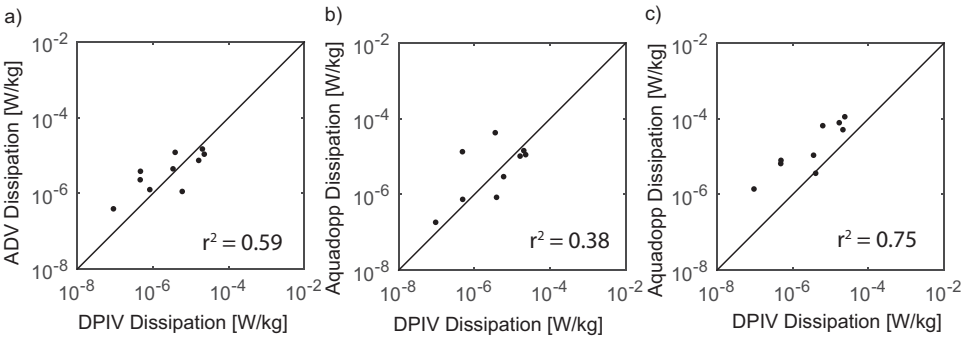

Figure 10. DPIV-derived TKE dissipation rates versus (a) that from the ADV at 3.35 m above the river bed, (b) that from the bottom Aquadopp at 1.83 m above the river bed, and (c) that from the bottom Aquadopp at 0.91 m above the river bed. The 1:1 line is shown in black.

correlation coefficients are reported for $\log_{10}(\varepsilon)$. The linear correlation coefficient is 0.59 between the surface ε and the ADV ε and 0.75 between the surface ε and the Aquadopp mounted at 0.91 m above the river bed. The correlation coefficient between the surface ε and the Aquadopp mounted at 1.83 m above the surface is of 0.38. The mostly strong correlation throughout the water column is expected due to the low stratification and low wind conditions described in section 3.1.

3.3. Surface Length-Scale Determined From Imagery and Correlation With Depth

As seen in Figure 4, the river surface is covered by warm features, depicted in lighter gray, surrounded by colder, darker filaments. The warm skin temperatures result from bulk water brought to the surface. The scale of these macroturbulent features seem to remain relatively constant over the duration of the 10 min runs allowing for surface length scales to be defined. The warm features are slightly anisotropic, often elongated in the direction of the flow. In some videos taken during the first night, reflection from the A-frame can be seen in the imagery as a cold artifact. These videos coincide with the period of time when the water column was more stratified and winds were stronger as noted in the previous section and are excluded from the subsequent analysis purely based on the presence of reflection.

For each run, a mean length scale was computed from *L1* and *L2*. Figure 11a shows a scatter plot of the length scales derived from the skin temperature fields versus water depth. The results show the scale of the surface features (*L*) is strongly linearly correlated ($r^2 = 0.88$) to the water depth (*D*), with a slope of (*D*/*L*) $\sim$ 13. As noted above, several outliers were excluded from this analysis and are not plotted in Figure 11. These outliers correspond to periods of time when the water column was more stratified and reflections dominated the temperature field. The correlation is slightly stronger ($r^2 = 0.93$) with *L2* which roughly corresponds to the direction of flow and weakly correlated with *L1* ($r^2 = 0.37$).

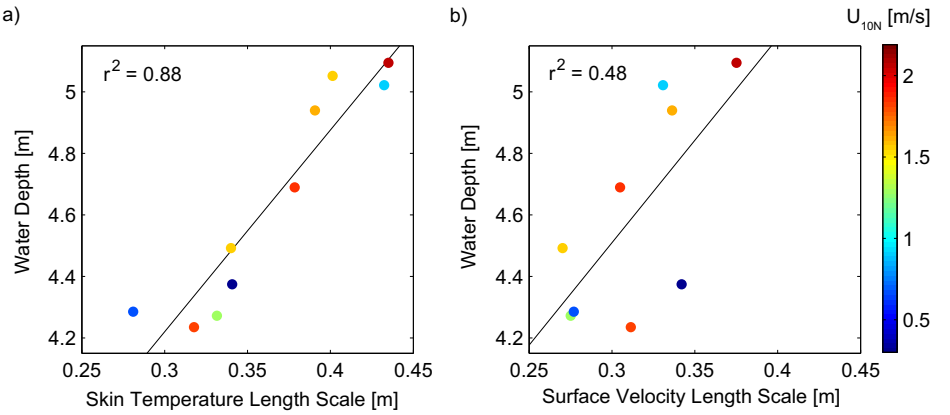

Figure 11. Scatter plot of the surface scales derived from the spatial autocorrelation functions of (a) the skin temperature and (b) the DPIV velocity fields against height of the water column. The data are color-coded according to wind speed (U_{10N}) and the black line shows the linear fit.

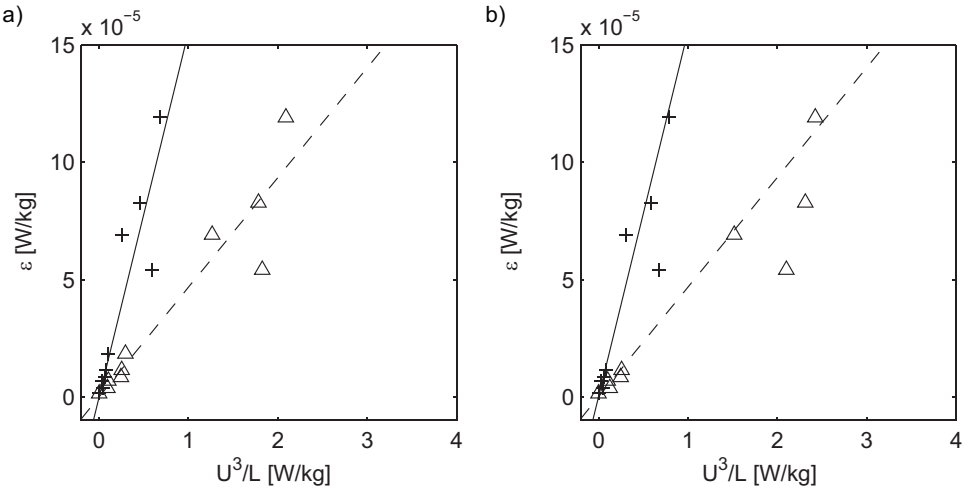

Figure 12. Scatter plots of the dissipation measured by the bottom Aquadopp against U^3/L where U is the mean velocity derived from the SAS (triangle) and DPIV (plus) and L is the temperature length scale in (a) and the DPIV scale in (b). The solid and dashed lines show the best fit of the form y = a*x when using the DPIV and SAS velocity, respectively. The proportionality coefficient or slope to the best fit in Figure 12a is 4.7 *10-5 for SAS and 1.6*10-4 for DPIV and in Figure 12b 3.9*10-6 for SAS and 1*10-4 for DPIV.

Although the mean length scale derived from the DPIV increases with water depth (cf. Figure 11b), the linear correlation is much smaller ($r^2 = 0.48$). On average, the mean DPIV scales are found to differ by ~7 cm from the temperature scales. This can mostly be attributed to the difference in resolution of the fields used to determine the scales. Indeed, the temperature scale has a pixel resolution i.e. ~0.8 cm, whereas the scale derived from the DPIV has a resolution of ~6.4 cm.

3.4. Determining Subsurface Dissipation Rates From Surface Current and Surface Length Scales

The turbulent kinetic energy dissipation rate can be estimated from the both the flow speed (U) and the dominant length scale in the flow (L). On the one hand, the dissipation rate equals the kinetic energy production rate which is proportional to U^2. One the other hand, the rate of kinetic energy supply can be thought as proportional to the inverse turnover time of large eddies: L/U. This implies $\varepsilon \sim \frac{U^2}{L/U} \sim \frac{U^3}{L}$ [*Tennekes and Lumley*, 1972]. As seen in Figure 12, $\frac{U^3}{L}$ computed from surface length scales and surface currents is highly linearly correlated to ε derive from the Aquadopp. Correlations are the strongest when using SAS velocities ($r^2 = 0.9$) and slightly lower when using DPIV ($r^2 = 0.82$) velocities. The strength of the correlation is comparable when the length scales derived directly from the temperature field or derived from the DPIV are used. Since the surface length scales L are highly correlated to D (see Figure10), the correlations are comparable. Using DPIV mean flow, we get $r^2 = 0.8$ and using SAS mean flow we get $r^2 = 0.86$. Note that while L varies by about 50%, $|u^3|$ spans three orders of magnitude. Therefore, it is the velocity magnitude and not L that controls the large variation in the dissipation rate and explains the major part of the high correlations coefficients found here. Indeed a quick sensitivity test shows that keeping U equal to the mean flow measured throughout the experiment and letting L vary, the correlations drop to $r^2 = 0.16$, whereas keeping L constant and varying U keeps correlations high with $r^2 = 0.77$–0.84.

4. Discussion

This study shows a clear linear relation between the scales of the surface temperature features and the water column depth. It also demonstrates that subsurface TKE dissipation rate can be estimated from surface length scales and mean flow speed. The ability to successfully determine subsurface and bulk flow properties from surface data is likely due to the low wind and weak stratification experienced during the measurement period. The agreement between the IR-derived mean surface current and subsurface velocities as well as the surface and subsurface TKE dissipation rate estimates suggest that the system was dominated by bottom-generated turbulence that propagated through the water column. Therefore, the bottom-generated turbulence governs properties of the TBL that are discernible in IR imagery. This is in agreement with the idea that in estuaries, under low wind conditions, turbulence is mainly tidally driven. Indeed, *Zappa*

et al. [2007] showed that for winds <5.5 m s^{-1}, the TKE dissipation rate near the surface (<38 cm) varied with tidal current. Although there is an apparent correlation between the length scales and the wind speed ($r^2 = 0.35$), the limited data available does not allow us to separate the wind speed effects from the depth dependence. Also, note that the strongest winds occurred during high tide. While the wind and tide should be independent of each other, the data were taken when the tidal elevation was highly correlated ($r^2 = 0.68$ in Figure 11) to the wind.

Under quiescent wind, elevated upward heat fluxes at the air-water interface lead to free convection [*Handler et al*., 2001; *Katsaros*, 1977; *Kudryavtsev and Soloviev*, 1985; *Volino and Smith*, 1999; *Zappa et al*., 1998]. This typically occurs during the night time when the near surface water experiences strong cooling. Although being a less energetic process than shear, free convection leads to disruption of the thermal boundary layer, with Bernard cells clearly detectable in IR imagery. When free convection dominates, the TKE dissipation rate is proportional to the buoyancy flux [*Lombardo and Gregg*, 1989]. The buoyancy flux estimated from the flux data measured at the piling using the COARE3.5 algorithm was not found to be correlated to the TKE dissipation ($r^2 = 0.1$) .However, the TKE dissipation rate was found to strongly correlate to the shear production ($\overline{u'w'}\frac{du}{dz}$ where the prime indicate the turbulent components of u and w the horizontal and flow vertical components, respectively) computed from the ADCP ($r^2 = 0.92$ for the deepest Aquadopp and $r^2 = 0.75$ for DPIV derived ε). Calculation of the momentum flux $\overline{u'w'}$ was done via Reynolds decomposition of the velocity components for each good subsurface ADCP bin over 10 min periods corresponding to times of IR image recording. The momentum flux was then multiplied by the horizontal shear between the depth above and below each bin to get the shear production. From these shear production profiles, we determined that both the bottom and the top, and as well as column mean shear production, were all highly correlated to the TKE dissipation rate. The correlation values reported above are for the column mean shear production.

The bulk shear (U/D) was found to be highly correlated both with surface dissipation estimates from the DPIV ($r^2 = 0.8$) and subsurface dissipation estimates from the Aquadopp ($r^2 = 0.78$). However, the surface temperature length scales where found to be only weakly correlated to the bulk shear ($r^2 = 0.19$–0.28 with the lowest for *L2* and the highest for *L*) and the shear production ($r^2 = 0.11$–0.32 with the lowest for *L1* and the highest for *L2*).

It is important to note here that the spectral models for turbulence used to estimate the TKE dissipation rates in this paper hinge on the assumption of isotropy [*Kolmogorov*, 1991]. However, at the surface, the kinematic boundary condition specifies a zero vertical velocity across the material surface. As *Talke et al*. [2013] discuss in spectral models on the assumption of "approximate isotropy." IR remote sensing for studies of estuarine and riverine turbulence as such environments are ubiquitously turbulent. *Chickadel et al*. [2011] have shown that IR derived dissipation rates correlate with in situ measured near-surface dissipation rate. They validate IR-derived ε with estimates from an ADV located 2 cm below the surface. While there were near surface dissipation measurements made during the current study, the surface estimates of dissipation are seen to reflect the deeper subsurface estimates of ε. *Chickadel et al*. [2011] made use of the Taylor hypothesis for the imagery estimates of ε, choosing to compute dissipation at a single location of the ADV at the surface. Our analysis suggests one can avoid having to assume the validity of the Taylor hypothesis. Our results show a strong correlation between surface and subsurface dissipation rate estimates from DPIV wavenumber spectra. Good correlation between DPIV dissipation rate estimates and near bottom ε is expected in a system dominated by bottom-generated turbulence. Surface modification of turbulence explains the order of magnitude difference between surface and near bottom ε. The lower correlation of midcolumn and surface ε is related to two high dissipation estimates of the Aquadopp. Recalculating the correlation coefficient without those outliers $r^2 = 0.89$.

Grid-turbulence experiments [*Batchelor*, 1953; *Sreenivasan*, 1984] in wind tunnels have provided evidence that at high Reynolds numbers, the TKE dissipation rate is independent of viscosity and when scaled by the integral length scale (L_i) and the root mean square velocity fluctuation (u') it is a constant of order unity: $\varepsilon = C_\varepsilon \frac{u'^3}{L_i}$ with $C_\varepsilon = 1$. This is in agreement with the Richardson-Kolmogorov cascade at equilibrium. In a recent review, *Vassilicos* [2015] report growing evidence of a nonequilibrium region where the TKE spectrum has Kolmogorov's $-5/3$ wave number and C_ε is a constant that depends on types of flow and boundary condition independently of Reynolds number. Here we show evidence of ε scaling as the cubed mean velocity rather than u'^3. This explains why the slopes in Figure 12 are not of order unity. Rather, the slope can be

related to an interfacial drag coefficient. Assuming a wall layer scaling for ε, the law of the wall dictates: $\varepsilon = \frac{u_*^3}{\kappa z}$, where u_* is the friction velocity, κ the von Kármán constant, and z the vertical distance from the wall. The drag coefficient (C_d) is defined as: $u_*^2 = C_d\ U^2$, where U is the mean velocity. It follows that: $\varepsilon = \frac{u_*^3}{\kappa z} = C_d^{\frac{3}{2}} \frac{U^3}{\kappa z}$ or $\varepsilon = C_d^{\frac{3}{2}} \beta \frac{U^3}{L} = C_{\varepsilon B} \frac{U^3}{L}$, where $\beta = \frac{L}{\kappa z}$ and $C_{\varepsilon B} = C_d^{\frac{3}{2}} \beta$ the bulk C_ε or slope in Figure 12. Figure 11, suggests that L/z is a constant of $O(10^{-2})$ giving a β of $O(10^{-1})$. Assuming a typical C_d over mud of $O(10^{-3})$ [*Gabioux et al*., 2005; *Trowbridge et al*., 1999], we derive a $C_{\varepsilon B}$ (or slope) of $O(10^{-5} - 10^{-6})$ for the data reported here.

The weak stratification of the water column is propitious for the transport of bottom-generated turbulence to the surface that disturbs the thermal boundary layer. The discernible surface temperature features that result allow for the observed relationship between the surface length scales and depth. As the system is tidally driven, the water depth and tidal velocity are related and out of phase. This suggests that the length scales are also related to the tidal velocity. However, the picture is complicated because study area was located outside the main channel where the water level and tidal current vary out of phase with a varying lag. Furthermore, due to the limited space sample available in this study, the effect of tidal asymmetry between ebb an flood could not be explored nor the how very slow currents around slack tide affect the surface length scales.

The relation between length scales and depth is likely to vary with the degree of stratification and may break down above some threshold. Under higher wind conditions, one could expect properties of the TBL to show less signature of bottom-generated turbulence. In a wind-driven TBL, there may be no boils discernible in IR imagery and the surface length scales would likely not be related to the water column depth. More data under higher wind conditions are necessary to verify the above statement.

Imagery taken during periods of stronger winds had to be excluded from the analysis because it was contaminated by reflections generated from small-scale surface gravity waves. Furthermore, even during periods of "enhanced" stratification, the *Ri* was mostly below 0.25 meaning that the degree of stratification did not vary enough to assess its potential effects on the results reported here. Therefore, the data available for the present study does not span a large enough variety of environmental conditions to determine objective criteria for when the skin temperature no longer shows signatures of bottom-generated turbulence. These objective criteria will include dependence on tidal current, stratification, net heat flux, surfactants, and wind speed. Since the temperature features studied here are generated at the river bed by the shear of the overflowing water, these would be observed once the flow is strong enough. There is therefore likely a minimum flow ($<$7 cm/s, according the data presented here) below which the results reported here are no longer valid. One could assume that once the velocity threshold has been exceeded depth becomes the limiting factor controlling *L*. Note that due to the limited parameter space sample of this tidal current threshold cannot be determined. Based on the study of *Zappa et al*. [2003] and *Zappa et al*. [2007], one could assume the results no longer to be valid for wind speeds exceeding 5.5 m s^{-1}. As for the degree of stratification, a feasible criterion could be based on the Richardson number, with the relation between length scale and depth likely to not hold for *Ri* greater than a critical value (Ri_c) somewhere between 1/4 and 1. The critical Richardson number was first determined for steady, two-dimensional, stably stratified, horizontal shear flows of an ideal Boussinesq fluid by *Miles* [1961] and [*Howard*, 1961] who determined that such flows are stable for $Ri > Ri_c = 1/4$ everywhere in the fluid. However, multiple studies [*Abarbanel et al*., 1984; *Geyer and Smith*, 1987; *Giddings et al*., 2011; *Nepf and Geyer*, 1996; *Tedford et al*., 2009] have found that Ri_c may be higher than the theoretical value and may lay anywhere between 0.2 and 1.0. Studying stratification in the Hudson River estuary *Nepf and Geyer* [1996] use $Ri_c < 0.4$ to indicate regions of potential mixing.

It is fair assume that scales observed at the surface may be as long as the water is deep. However it is important to note that the footprint of the IR imagery is only 2–3 m whereas the water depth is 4–5 m. This means that those larger scales are not captured in this study. Indeed, wavenumber spectra of the imagery (not shown) reveal no leveling or drop of energy at the lowest wavenumbers observed, suggesting that there is significant energy at higher scales than those captured in our limited field of view. A much larger footprint would be needed such as can easily be obtained from airborne platforms. Analysis of ADV spectra showed inconsistent roll off at low wavenumbers but also hint to existence of turbulent scales larger than the field of view. Clear peaks were detected in a small number of ADV wavenumber spectra at length scales of *O*(1–10 m), an example of which is seen in Figure 3. This hints to the presence of subsurface coherent structures of similar scale as those detected at the surface.

The relation between the length scales and the water depth shown here differs in magnitude to that reported in previous studies. The scales reported here are decorrelation lengths and represent the radius of surface coherent structures rather than the diameter which is typically reported. Further discrepancies could be explained by the different origin of the signal observed. Here, a temperature signal is detected, whereas previous work was based on visual and acoustic observations of boil diameters or on flow visualizations of eddies and surface velocity field derived length scales. No boils were visually observed during the field experiment. This suggests that the scales reported here while being intrinsic scales of bottom-generated turbulence are unlikely associated with boils. Length scales associated with disruption of the thermal boundary layer, with counterrotating vortices detected in the flow field, and with boils observed with the naked eye may differ significantly even though all signatures evolved from bottom-generated turbulence. As these scales all seem to be related to depth, it should be possible to find a unifying relationship between them. A first guess could be deduced from previous studies, but simultaneous observation would be required to verify it.

One could expect velocity scales related to boils scales to be half the temperature length scales. This is because the velocity anomaly will go to zero at the center of the boil and outside, while the temperature has a single minimum. Our data does not, however, show such a relation between the temperature and velocity scales. This is related to the inability to measure the largest integral scale given our limited image size. Early observations in the Polomet River Russia, where depth varied 0.7 and 2.1 m [*Korchokha*, 1968] suggest that D/d lies between 3.7 and 1.75, where D is the water depth and d boil diameter. *Jackson* [1976] documented boils of up to 2–4 m diameter in lower Wabash River where depth ranged from 0.7 to 5.6 m, suggesting $D/d \sim 2.5$. *Nimmo-Smith et al*. [1999] reported boils in a well-mixed and tidal region of the North Sea where depth ranged from 17 to 33 m. Covering 20–30% of surface, the boil diameters seen in visible images were 1.04–1.44 times the water depth. They also determined boils size from an upward-pointing side scan sonar mounted on the sea floor, based on the backscatter of bubble accumulating in surface convergence. The diameters measured acoustically were around 0.93 times D.

Early flow visualization work by [*Klaven*, 1966, 1968; *Klaven and Kopaliani*, 1973] in a 0.05 m deep water columns, suggested the presence of eddies or stream wise counter rotating vortices with vertical scales equal to the water depth and lengths of 4–7 times the water depth for rough and smooth beds, respectively. Further flow visualization laboratory experiments by *Shvidchenko and Pender* [2001] performed in 0.025–0.1 m depth suggested an average eddy length of 4.5 times the water depth. In a more recent study, *Johnson and Cowen* [2014] computed the length scales associated with such eddies from visible imagery using PIV-derived flow fields. They report the transverse and stream wise length scale as $0.5D$ and $2.5D$, respectively for water depth ranging from 10 to 30 cm.

Johnson and Cowen [2014] also showed that the length scale normalized by the flow depth is linearly dependent on the turbulent Reynolds number ($Re_T = \frac{UL}{\nu}$, where U is the current speed). The Hudson River data (cf. Table 1) suggest a weak linear correlation between L/D and Re_T ($r^2 = 0.44$). The correlation is equally weak ($r^2 = 0.45$) between L and the bulk Reynolds number ($Re = \frac{UD}{\nu}$). One could expect the surface features not only to depend on bulk water column properties, but also on surface generated turbulence, mainly on wind speed. However, under the low wind conditions experienced during this field experiment, variation in the wind only accounts for 35 percent of the variation in length scale.

Several factors affect the burst cycle and the evolution of subsequent coherent structures. Bed roughness was found to affect the inner layer. *Grass* [1971] observed how rough beds lead to less copious wall streaks. However, periodic energetic growth and breakups were observed over both rough and smooth beds. Multiple studies reported [e.g., *Matthes*, 1947] that the presence of suspended sediment leads to dampened turbulence. Whether suspended sediments would lead to less frequent or to smaller kolks and eddies traveling toward the surface could have significant impact on the surface signature of bottom-generated turbulence and potentially alter the proportionality factor between surface length scales and water column depth. Finally, surface waves and especially breaking wave overwhelm less turbulent structures of bursting. In such unsteady flow fields, bursting and its surface signature may not be recognizable.

5. Conclusions

The strong linear relation between surface length scale determined from IR imagery and water column depth is a promising result and should be explored further in a variety of environments. The ability to

remotely derive bathymetry is also valuable for estimating river discharge as suggested by *Johnson and Cowen* [2014]. Using IR imagery offers an advantage over visible imagery as it has been shown that DPIV and SAS algorithms can directly be applied to the IR imagery to get surface velocities without needing to seed the water. DPIV flow fields can be used to estimate surface dissipation rates from IR imagery. These surface dissipation rates estimate subsurface dissipation in tidally driven systems under low wind and weak stratification. Under such conditions, it is also possible to determine subsurface dissipation rates from surface length scales and a mean flow using $\varepsilon \sim \frac{U^3}{L}$. Although imagery analyzed here was taken from a barge, the methods used can easily adaptable to a variety of potential platforms including helicopters, aircraft, and unmanned air systems, as well as fixed platforms.

Acknowledgments
The authors wish to thank Kenneth Vierra, Mike Marnon, Kyle Bisson, and Zandy Williams from Areté Associates for their assistance and support during the field work in Hudson River. The authors thank Deborah LeBel for assistance with data processing specifically the subsurface dissipation estimates. The authors thank Miller's Launch for providing the crew boat Marguerite Miller and for their assistance on board. The authors also gratefully acknowledge support from the Office of Naval Research Awards N00014-11-1-0922 and N00014-15-1-2153 for the Lamont-Doherty Earth Observatory and N00014-13-C-0387 for Areté Associates. The data can be provided by Chris Zappa (email: zappa@ldeo.columbia.edu). This is Lamont-Doherty Earth Observatory contribution #7975.

References

Abarbanel, H. D. I., D. D. Holm, J. E. Marsden, and T. Ratiu (1984), Richardson-number criterion for the nonlinear stability of 3-dimensional stratified flow, *Phys. Rev. Lett.*, *52*(26), 2352–2355.
Abood, K. A. (1974), Circulation in the Hudson estuary, *Ann. N. Y. Acad. Sci.*, *250*(1), 39–111.
Adrian, R., C. Meinhart, and C. Tomkins (2000), Vortex organization in the outer region of the turbulent boundary layer, *J. Fluid Mech.*, *422*, 1–54.
Allen, J. R. L. (1985), *Principles of Physical Sedimentology*, George Allen and Unwin, London, U. K.
Batchelor, G. K. (1953), *The Theory of Homogeneous Turbulence*, Cambridge Univ. Press, Cambridge.
Bell, R. E., et al. (2006), Benthic habitat mapping in the Hudson River Estuary, in edited by J. Levinton and J. Waldman, pp. 51–64, *The Hudson River Estuary*, Cambridge University Press, Cambridge.
Best, J. (2005), The fluid dynamics of river dunes: A review and some future research directions, *J. Geophys. Res.*, *110*, F04S02, doi:10.1029/2004JF000218.
Chickadel, C. C., A. R. Horner-Devine, S. A. Talke, and A. T. Jessup (2009), Vertical boil propagation from a submerged estuarine sill, *Geophys. Res. Lett.*, *36*(10).
Chickadel, C. C., S. A. Talke, A. R. Horner-Devine, and A. T. Jessup (2011), Infrared-based measurements of velocity, turbulent kinetic energy, and dissipation at the water surface in a tidal river, *IEEE Geosci. Remote Sens. Lett.*, *8*(5), 849–853.
Dugan, J. P., and C. C. Piotrowski (2012), Measuring currents in a coastal inlet by advection of turbulent eddies in airborne optical imagery, *J. Geophys. Res.*, *117*, C03020, doi:10.1029/2011JC007600.
Dugan, J. P., S. P. Anderson, C. C. Piotrowski, and S. B. Zuckerman (2014), Airborne infrared remote sensing of riverine currents, *IEEE Trans. Geosci. Remote Sens.*, *52*(7), 3895–3907.
Farrar, J. T., C. J. Zappa, R. A. Weller, and A. T. Jessup (2007), Sea surface temperature signatures of oceanic internal waves in low winds, *J. Geophys. Res.*, *112*, C06014, doi:10.1029/2006JC003947.
Gabioux, M., S. B. Vinzon, and A. M. Paiva (2005), Tidal propagation over fluid mud layers on the Amazon shelf, *Cont. Shelf Res.*, *25*(1), 113–125.
Geyer, W. R., and J. D. Smith (1987), Shear instability in a highly stratified estuary, *J. Phys. Oceanogr.*, *17*(10), 1668–1679.
Giddings, S. N., D. A. Fong, and S. G. Monismith (2011), Role of straining and advection in the intratidal evolution of stratification, vertical mixing, and longitudinal dispersion of a shallow, macrotidal, salt wedge estuary, *J. Geophys. Res.*, *116*, C03003, doi:10.1029/2010JC006482.
Gordon, C. M. (1975), Sediment entrainment and suspension in a turbulent tidal flow, *Marine Geology*, *18*(1), M57–M64.
Grass, A. J. (1971), Structural features of turbulent flow over smooth and rough boundaries, *J. Fluid Mech.*, *50*(2), 233–255.
Handler, R. A., G. B. Smith, and R. I. Leighton (2001), The thermal structure of an air-water interface at low wind speeds, *Tellus Ser. A*, *53*, 233–244.
Heathershaw, A. D. (1974), "Bursting" phenomena in the sea, *Nature*, *248*(5447), 394–395.
Howard, L. N. (1961), Note on a paper of miles, John, W., *J. Fluid Mech.*, *10*(4), 509–512.
Hurther, D., U. Lemmin, and E. A. Terray (2007), Turbulent transport in the outer region of rough-wall open-channel flows: The contribution of large coherent shear stress structures (LC3S), *J. Fluid Mech.*, *574*(1), 465–493.
Jackson, R. G. (1976), Sedimentological and fluid-dynamic implications of the turbulent bursting phenomenon in geophysical flows, *J. Fluid Mech.*, *77*(3), 531–560.
Johnson, E. D., and E. A. Cowen (2014), Remote monitoring of volumetric discharge based on surface mean and turbulent metrics, paper presented at River Flow 2014: The 7th International Conference on Fluvial Hydraulics, École Polytechnique Fédérale de Lausanne, Lausanne.
Katsaros, K. B. (1977), The sea surface temperature deviation at very low wind speeds; Is there a limit?, *Tellus*, *29*(3), 229–239.
Katsaros, K. B. (1980), The aqueous thermal boundary layer, *Boundary Layer Meteorol.*, *18*, 107–127.
Klaven, A. B. (1966), Investigation of the flow turbulent structure [in Russian], *Trans. State Hydrol. Inst.*, *136*, 65–76.
Klaven, A. B. (1968), Kinematic structure of the turbulent flow (in Russian), *Trans. State Hydrol. Inst.*, *147*, 134–141.
Klaven, A. B., and Z. D. Kopaliani (1973), Laboratory investigations of the kinematic structure of turbulent flow over a rough bed [in Russian], *Trans. State Hydrol. Inst.*, *209*, 67–90.
Kline, S. J., W. C. Reynolds, F. A. Schraub, and P. W. Runstadler (1967), The structure of turbulent boundary layers, *J. Fluid Mech.*, *30*(4), 741–773.
Kolmogorov, A. N. (1991), Dissipation of energy in the locally isotropic turbulence, *Proceedings: Mathematical and Physical Sciences*, *434*(1890), 15–17.
Korchokha, Y. (1968), Investigation of the dune movement of sediments on the Polomet River, *Sov. Hydrol. Sel.*, *6*, 541–559.
Kudryavtsev, V. N., and A. V. Soloviev (1985), On the parameterization of the cold film on the ocean surface, *Izv. Acad. Sci. USSR, Atmos. Ocean Phys.*, *21*(2), 177–183.
Leibovich, S. (1983), The form and dynamics of Langmuir circulations, *Annu. Rev. Fluid Mech.*, *15*, 391–427.
Liu, W. T., and J. A. Businger (1975), Temperature profile in the molecular sublayer near the interface of a fluid in turbulent motion, *Geophys. Res. Lett.*, *2*(9), 403–404.

Lombardo, C., and M. Gregg (1989), Similarity scaling of viscous and thermal dissipation in a convecting surface boundary layer, *J. Geophys. Res.*, *94*(C5), 6273–6284.
Matthes, G. H. (1947), Macroturbulence in natural stream flows, Eos, Transactions American Geophysical Union, *28*(2), 255–265.
McKenna, S. P., and W. R. McGillis (2002), Performance of digital image velocimetry processing techniques, *Exp. Fluids*, *32*, 116–115.
Melville, W. K., R. Shear, and F. Veron (1998), Laboratory measurements of the generation and evolution of Langmuir circulations, *J. Fluid Mech.*, *364*, 31–58.
Miles, J. W. (1961), On the stability of heterogeneous shear flows, *J. Fluid Mech.*, *10*(4), 496–508.
Nepf, H. M., and W. R. Geyer (1996), Intratidal variations in stratification and mixing in the Hudson estuary, *J. Geophys. Res.*, *101*(C5), 12,079–12,086.
Nezu, I., and H. Nakagawa (1993), *Turbulence in Open Channels, IAHR/AIRH Monograph*, Balkema, Rotterdam, Netherlands.
Nimmo-Smith, W. A. M., S. A. Thorpe, and A. Graham (1999), Surface effects of bottom-generated turbulence in a shallow tidal sea, *Nature*, *400*, 251–254.
Offen, G. R., and S. J. Kline (1975), A proposed model of the bursting process in turbulent boundary layers, *J. Fluid Mech.*, *70*(2), 209–228.
Plant, W. J., et al. (2009), Remotely sensed river surface features compared with modeling and in situ measurements, *J. Geophys. Res.*, *114*, C11002, doi:10.1029/2009JC005440.
Puleo, J. A., T. E. McKenna, K. T. Holland, and J. Calantoni (2012), Quantifying riverine surface currents from time sequences of thermal infrared imagery, *Water Resour. Res.*, *48*, W01527, doi:10.1029/2011WR010770.
Saunders, P. M. (1967), The temperature at the ocean-air interface, *J. Atmos. Sci.*, *24*, 269–273.
Shvidchenko, A. B., and G. Pender (2001), Macroturbulent structure of open-channel flow over gravel beds, *Water Resour. Res.*, *37*(3), 709–719.
Smith, G. B., R. J. Volino, R. A. Handler, and R. I. Leighton (2001), The thermal signature of a vortex pair impacting a free surface, *J. Fluid Mech.*, *444*, 49–78.
Sreenivasan, K. R. (1984), On the scaling of the turbulence energy dissipation rate, *Phys. Fluids*, *27*(5), 1048–1051.
Talke, S. A., A. R. Horner-Devine, C. C. Chickadel, and A. T. Jessup (2013), Turbulent kinetic energy and coherent structures in a tidal river, *J. Geophys. Res. Oceans*, *118*, 6965–6981, doi:10.1002/2012JC008103.
Tedford, E. W., J. R. Carpenter, R. Pawlowicz, R. Pieters, and G. A. Lawrence (2009), Observation and analysis of shear instability in the Fraser River estuary, *J. Geophys. Res.*, *114*, C11006, doi:10.1029/2009JC005313.
Tennekes, H., and J. L. Lumley (1972), *A First Course in Turbulence*, MIT Press, Cambridge, Mass.
Trowbridge, J. H., W. R. Geyer, M. M. Bowen, and A. J. Williams (1999), Near-bottom turbulence measurements in a partially mixed estuary: Turbulent energy balance, velocity structure, and along-channel momentum balance*, *J. Phys. Oceanogr.*, *29*(12), 3056–3072.
Vanoni, V. A., L. S. Hwang (1967), Relation between bed forms and friction in streams, *J. Hydraul. Div.*, ASCE, *93*(HY3), 121–144.
Vassilicos, J. C. (2015), Dissipation in turbulent flows, *Annu. Rev. Fluid Mech.*, *47*, 95–114.
Veron, F., and W. K. Melville (2001), Experiments on the stability and transition of wind-driven water surfaces, *J. Fluid Mech.*, *446*, 25–65.
Veron, F., W. K. Melville, and L. Lenain (2008), Infrared techniques for measuring ocean surface processes, *J. Atmos. Oceanogr. Technol.*, *25*(2), 307–326.
Veron, F., W. K. Melville, and L. Lenain (2009), Measurements of ocean surface turbulence and wave–turbulence interactions, *J. Phys. Oceanogr.*, *39*, 2310–2323, doi:10.1175/2009JPO4019.1.
Volino, R. J., and G. B. Smith (1999), Use of simultaneous IR temperature measurements and DPIV to investigate thermal plumes in a thick layer cooled from above, *Experiments in fluids*, *27*(1), 70–78
Yalin, M. S. (1992), *River Mechanics*, 219 pp., Elsevier, N. Y.
Zappa, C. J., and A. T. Jessup (2005), High resolution airborne infrared measurements of ocean skin temperature, *Geosci. Remote Sens. Lett.*, *2*(2), 146–150, doi:10.1109/LGRS.2004.841629.
Zappa, C. J., A. T. Jessup, and H. H. Yeh (1998), Skin-layer recovery of free-surface wakes: Relationship to surface renewal and dependence on heat flux and background turbulence, *J. Geophys. Res.*, *103*(C10), 21,711–21,722.
Zappa, C. J., P. A. Raymond, E. A. Terray, and W. R. McGillis (2003), Variation in surface turbulence and the gas transfer velocity over a tidal cycle in a macro-tidal estuary, *Estuaries*, *26*(6), 1401–1415.
Zappa, C. J., W. E. Asher, A. T. Jessup, J. Klinke, and S. R. Long (2004), Microbreaking and the enhancement of air-water transfer velocity, *J. Geophys. Res.*, *109*, C08S16, doi:10.1029/2003JC001897.
Zappa, C. J., W. R. McGillis, P. A. Raymond, J. B. Edson, E. J. Hintsa, H. J. Zemmelink, J. W. H. Dacey, and D. T. Ho (2007), Environmental turbulent mixing controls on the air-water gas exchange in marine and aquatic systems, *Geophys. Res. Lett.*, *34*, L10601, doi:10.1029/2006GL028790.